

SCC-Loc: A Unified Semantic Cascade Consensus Framework for UAV Thermal Geo-Localization

Xiaoran Zhang, Yu Liu, Jinyu Liang, Kangqiushi Li, Zhiwei Huang, Huaxin Xiao*

Abstract—Cross-modal Thermal Geo-localization (TG) provides a robust, all-weather solution for Unmanned Aerial Vehicles (UAVs) in Global Navigation Satellite System (GNSS)-denied environments. However, profound thermal-visible modality gaps introduce severe feature ambiguity, systematically corrupting conventional coarse-to-fine registration. To dismantle this bottleneck, we propose SCC-Loc, a unified Semantic-Cascade-Consensus localization framework. By sharing a single DINOv2 backbone across global retrieval and MINIMA_{RoMa} matching, it minimizes memory footprint and achieves zero-shot, highly accurate absolute position estimation. Specifically, we tackle modality ambiguity by introducing three cohesive components. First, we design the Semantic-Guided Viewport Alignment (SGVA) module to adaptively optimize satellite crop regions, effectively correcting initial spatial deviations. Second, we develop the Cascaded Spatial-Adaptive Texture-Structure Filtering (C-SATSF) mechanism to explicitly enforce geometric consistency, thereby eradicating dense cross-modal outliers. Finally, we propose the Consensus-Driven Reliability-Aware Position Selection (CD-RAPS) strategy to derive the optimal solution through a synergy of physically constrained pose optimization. To address data scarcity, we construct Thermal-UAV, a comprehensive dataset providing 11,890 diverse thermal queries referenced against a large-scale satellite ortho-photo and corresponding spatially aligned Digital Surface Model (DSM). Extensive experiments demonstrate that SCC-Loc establishes a new state-of-the-art, suppressing the mean localization error to 9.37 m and providing a 7.6-fold accuracy improvement within a strict 5-m threshold over the strongest baseline. Code and dataset are available at <https://github.com/FloralHercules/SCC-Loc>.

Index Terms—Unmanned Aerial Vehicles, Cross-View Image Geolocation, Multimodal Image Registration, Thermal Imagery, Vision Foundation Models.

I. INTRODUCTION

WITH the rapid advancement of multimodal remote sensing and Earth observation technologies, Unmanned Aerial Vehicles (UAVs) have emerged as indispensable platforms for various aerial surveying and monitoring applications. However, the autonomous operation of these platforms in Global Navigation Satellite System (GNSS)-denied environments heavily relies on robust and accurate self-localization [1], [2]. Visual Geo-localization (VG) has emerged as a promising solution to bridge this gap. At its core, VG determines precise geographical coordinates by establishing robust cross-view image registration and multiview matching

Xiaoran Zhang, Yu Liu, Jinyu Liang, Kangqiushi Li, Zhiwei Huang, and Huaxin Xiao are with the College of Systems Engineering, National University of Defense Technology, Changsha 410073, China (Corresponding author: Huaxin Xiao; e-mail: {zhangxiaoran, liuyu20, liangjinyu24, likangqiushi20, huangzhiwei21, xiaohuaxin}@nudt.edu.cn).

This work has been submitted to the IEEE for possible publication. Copyright may be transferred without notice, after which this version may no longer be accessible.

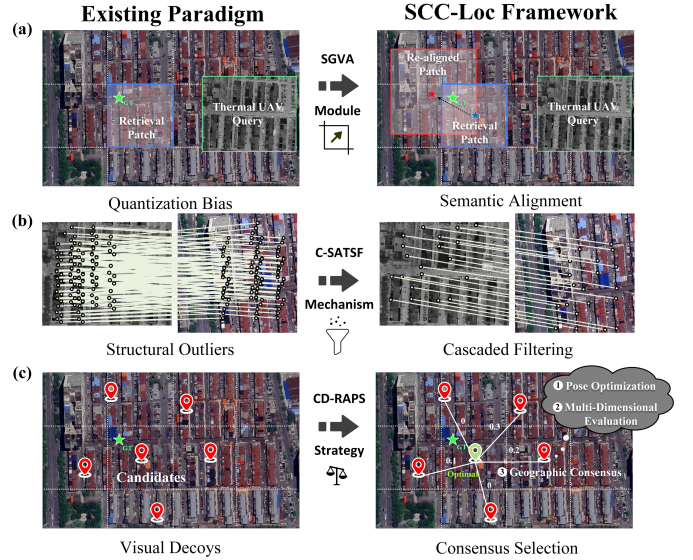


Fig. 1. Conceptual comparison of the existing paradigm and our SCC-Loc framework. To overcome severe cross-modal bottlenecks in thermal geo-localization, SCC-Loc systematically resolves: (a) spatial quantization bias via semantic alignment (SGVA); (b) dense structural outliers via cascaded filtering (C-SATSF); and (c) deceptive visual decoys via consensus selection (CD-RAPS).

between onboard camera imagery and geo-referenced satellite maps [3], [4].

Despite its tremendous potential, conventional visible-light VG is fundamentally constrained by its reliance on photometric consistency, leading to catastrophic performance degradation under severe illumination variations and nighttime conditions [5]. To break this limitation and enable true day-and-night all-weather autonomy, cross-modal Thermal Geo-localization (TG) has recently attracted significant attention [5], [6], [7]. By exploiting illumination-invariant thermal infrared imagery and matching it against widely available visible-light satellite databases, TG offers a highly resilient alternative. Nevertheless, establishing reliable spatial correspondences across these highly heterogeneous domains remains a formidable cross-modal remote sensing challenge.

To achieve precise self-localization across large-scale global satellite maps, state-of-the-art geo-localization frameworks almost exclusively adopt a coarse-to-fine hierarchical paradigm [8], [9], [10]. This standard pipeline operates by first employing global image retrieval to isolate candidate regions (coarse localization), subsequently relying on local feature matching to establish dense spatial correspondences for precise coordinate estimation (fine localization).

Despite the success of these two-stage methods on standard homologous visible-light benchmarks, shifting their application directly to cross-modal thermal-to-visible matching exposes unprecedented challenges. Because thermal radiation and solar reflectance differ fundamentally in their physical imaging mechanisms, this profound modality gap obliterates critical local textures and structural invariants essential to conventional matching algorithms [6], [11]. Consequently, direct deployment of this conventional pipeline in complex, real-world cross-modal scenarios triggers three critical bottlenecks, as conceptually illustrated in Fig. 1:

- **Spatial quantization bias induces fatal viewport misalignments (Fig. 1(a)).** Traditional retrieval relies on databases constructed via discretized sliding windows [12], [13]. Because these fixed grid centers rarely align with actual UAV positions, target regions are frequently marginalized or truncated. In texture-sparse thermal imagery, such initial spatial errors fatally deprive the subsequent fine-matching stage of sufficient overlapping regions.
- **Modality discrepancies generate massive structural outliers (Fig. 1(b)).** Thermal imagery’s inherent texture deficit induces severe feature ambiguity, forcing conventional matchers to overly cluster points in high-contrast areas [11]. Furthermore, repetitive topological patterns (e.g., identical rooftops) produce widespread spurious correspondences that exhibit local structural similarity but lack global geometric rigidity. Directly utilizing these contaminated matches for pose estimation inevitably leads to catastrophic localization failures.
- **Visual decoys restrain robust optimal position selection (Fig. 1(c)).** In large-scale search spaces, macroscopic structural repetitions frequently yield deceptively high inlier counts for entirely incorrect locations. Existing methods merely rely on the number of inlier counts to select the best candidate pose, while falling into the “low residual, high drift” trap induced by these visual decoys [9].

To bypass these conventional matching bottlenecks, some pioneering thermal-specific networks (e.g., STHN [6]) attempt to learn cross-modal mappings through domain-specific training. However, they heavily rely on a data-hungry supervised paradigm [14], [15], [16]. This inherently limits their zero-shot generalization capabilities, causing them to overfit to narrow scenarios and struggle when deployed in unseen environments. Moreover, they are highly sensitive to initial rotational misalignments against satellite maps caused by telemetry noise, severely hindering robust real-world navigation.

Furthermore, the vulnerability of such data-hungry models is severely exacerbated by critical data scarcity. Currently, the academic community relies almost exclusively on a single open-source cross-modal dataset, *Boson-nighttime* [5]. However, this dataset exhibits severe limitations: it overly focuses on homogeneous scenes like deserts while lacking complex urban and rural topologies, and it is strictly confined to purely nighttime conditions, failing to capture diurnal thermal variations. This dual absence of spatial diversity and temporal

span makes supervised cross-modal models highly prone to overfitting, impeding the comprehensive evaluation of localization algorithms in real-world environments.

To address these challenges, we propose SCC-Loc, a unified Semantic-Cascade-Consensus framework for seamless coarse-to-fine thermal geo-localization. Unlike disjointed paradigms that suffer from error accumulation, SCC-Loc explicitly tackles the cross-modal bottlenecks through a highly cohesive pipeline: it adaptively aligns spatial viewports via semantic guidance, progressively purifies structural outliers through a cascaded sieve, and integrates physically constrained optimization, multi-dimensional evaluation, and geographic consensus voting to deduce the optimal position. Furthermore, to bridge the benchmarking gap in this domain, we construct and introduce a comprehensive Thermal-UAV dataset, providing a rigorous real-world testbed for cross-modal localization.

The main contributions of this paper are summarized as follows:

- We propose SCC-Loc, a highly cohesive pipeline that explicitly tackles cross-modal bottlenecks and systematically bridges the semantic, structural, and geographic gaps in thermal geo-localization.
- We design the SGVA module. By exploiting high-level semantic activations from a shared DINOv2 backbone to adaptively optimize the crop center, it actively corrects misalignments and effectively resolves the critical spatial quantization bias.
- We introduce the C-SATSF mechanism. Acting as a hierarchical sieve, it rigorously enforces spatial equalization, texture verification, and structure-consistent refinement to progressively strip away massive outliers and distill a highly dependable correspondence set.
- We propose the CD-RAPS strategy. To overcome the “low residual, high drift” trap caused by visual decoys, it integrates physically constrained non-linear optimization with multi-dimensional reliability evaluation and geographic consensus voting.
- We construct Thermal-UAV, a diverse cross-modal dataset featuring day-night variations and complex urban-rural scenes. Extensive experiments demonstrate that SCC-Loc comprehensively outperforms existing state-of-the-art baselines on this benchmark, significantly reducing the mean localization error and establishing a new paradigm for robust all-weather UAV positioning.

The remainder of this paper is organized as follows: Section II reviews existing literature on UAV visual geo-localization. Section III details the proposed SCC-Loc framework and its core modules. Section IV describes the dataset construction, evaluation metrics, baseline methods, and implementation details. Section V presents the comprehensive experimental results. Section VI discusses the research findings and outlines future avenues. Finally, Section VII concludes this work.

II. RELATED WORK

UAV Visual Geo-localization (VG) aims to retrieve absolute global coordinates by matching onboard imagery with geo-

referenced satellite maps. Following the technological evolution, existing approaches can be categorized into cross-view image retrieval for coarse localization, fine-grained visual positioning, coarse-to-fine hierarchical frameworks, and the emerging thermal-based geo-localization.

A. Cross-View Image Retrieval for Coarse Localization

Retrieval-based methods formulate localization as a metric learning task to search for nearest neighbors in satellite databases [17], [18], [19]. Early research focused on backbone evolution and semantic alignment, with Zheng et al. [3] establishing the University-1652 benchmark. To overcome CNN receptive field limitations, FSRA [20] utilized Transformers for long-range dependency capture. Building upon this, CAMP [21] introduced position-aware partitioning for layout-consistent representations, while SeGCN [22] leveraged Graph Convolutional Networks to explicitly model the topological relationships of semantic regions against viewpoint shifts.

Recently, Visual Foundation Models (VFMs) have introduced an off-the-shelf paradigm [12], [23], [24]. AnyLoc [23] employs self-supervised DINOv2 features with VLAD for robust zero-shot retrieval, while UAVPlace [12] explicitly encodes rotation and scale perturbations to bolster descriptor invariance. Pushing these boundaries, DINOv3 [24] further scales representation learning for unprecedented robustness and dense semantic alignment. While effective for image-level recognition, these VFM-based methods remain limited to discrete topological outputs, failing to satisfy the demand for continuous and precise spatial coordinate estimation.

B. Fine-Grained Visual Position Estimation

To achieve precise localization, researchers have developed methods based on feature matching and direct regression. Traditional template matching (e.g., NCC [25]) often fails under drastic illumination changes, whereas early deep learning-based matchers (e.g., SuperPoint [26], LoFTR [27]) have significantly improved robustness by establishing pixel-level 2D-2D correspondences. Building on this, more recent robust matching architectures like RoMa [28] leverage dense feature correlation to handle extreme viewpoint and illumination variations. Furthermore, to specifically overcome the severe appearance variations across heterogeneous data, cross-modal matchers such as XoFTR [11] and adaptive matching frameworks like MINIMA [29] have been introduced, enabling reliable feature associations even under significant modality gaps.

Alternatively, recent approaches formulate geo-localization as an end-to-end regression task to directly predict spatial offsets. For instance, OS-FPI [30] employs a one-stream architecture that couples classification with offset regression for fine-grained localization. Advancing this paradigm, MMGLT [31] leverages a multimodal Transformer to regress geographic coordinates within a local search region. Although these regression-based methods yield high precision, they intrinsically rely on restrictive assumptions regarding the initial search area (i.e., requiring a known prior location) and remain highly vulnerable to large-scale cross-modal scene variations.

C. Coarse-to-Fine Hierarchical Localization

To balance search scope with localization precision, the coarse-to-fine two-stage strategy has become the prevailing paradigm [8]. Typical frameworks, such as AirGeoNet [10] and AnyVisLoc [9], adopt a modular coupling design: candidate satellite patches are first retrieved, followed by fine coordinate solving within these regions using local feature matching or semantic alignment. For instance, Meng et al. [10] achieved robust 3-DOF pose estimation by performing dense convolutional matching between aerial features and rasterized 2D semantic maps. Furthermore, Ye et al. [9] established a unified benchmark integrating image retrieval, pixel-level matching, and Digital Surface Model (DSM)-based Perspective-n-Point (PnP) solving. However, existing two-stage methods often suffer from a disjoint design. The coarse and fine stages typically rely on independent feature extractors, leading to doubled space consumption and computational redundancy.

D. Thermal-Based UAV Geo-localization

While the aforementioned methods have achieved remarkable progress in RGB imagery, they inevitably experience severe performance degradation or total failure under illumination-deprived conditions (e.g., nighttime, dense fog, or smog). Consequently, leveraging thermal infrared sensors has emerged as a crucial alternative. Nevertheless, thermal-based absolute visual localization is fundamentally challenged by a severe modality gap: thermal images reflect temperature radiation (characterized by low texture and high self-similarity), whereas satellite maps depict visible light reflectance [32], [33].

Pioneering this field, Xiao et al. [5] introduced the Boson-nighttime dataset—a benchmark predominantly featuring homogeneous nighttime desert environments. They proposed a dual-module framework utilizing a Thermal Generative Module (TGM) to synthesize pseudo-thermal images for subsequent Satellite-Thermal Geo-localization Module (SGM) retrieval. To advance beyond coarse retrieval, they subsequently developed STHN [6], a deep homography network for thermal-satellite alignment. This was later augmented by UASTHN [7], utilizing uncertainty-aware Crop-based Test-Time Augmentation (CropTTA) to reject unreliable matches. Concurrently, Liu et al. [34] designed NIVnet, neutralizing modality discrepancies by disentangling features into shared shape and specific attribute subspaces.

Limitations & Our Motivation: Despite these trailblazing efforts, current thermal-based approaches heavily rely on domain-specific training using paired thermal-satellite data. This data-hungry paradigm inherently limits their *generalization* capabilities, causing them to overfit to narrow scenarios and struggle when deployed in unseen environments. This vulnerability is further exacerbated by the scarcity of diverse thermal benchmarks, as existing datasets are predominantly confined to single regions (e.g., deserts) and limited time-frames.

To break this bottleneck, we tackle these limitations from both data and algorithmic perspectives. First, to address the

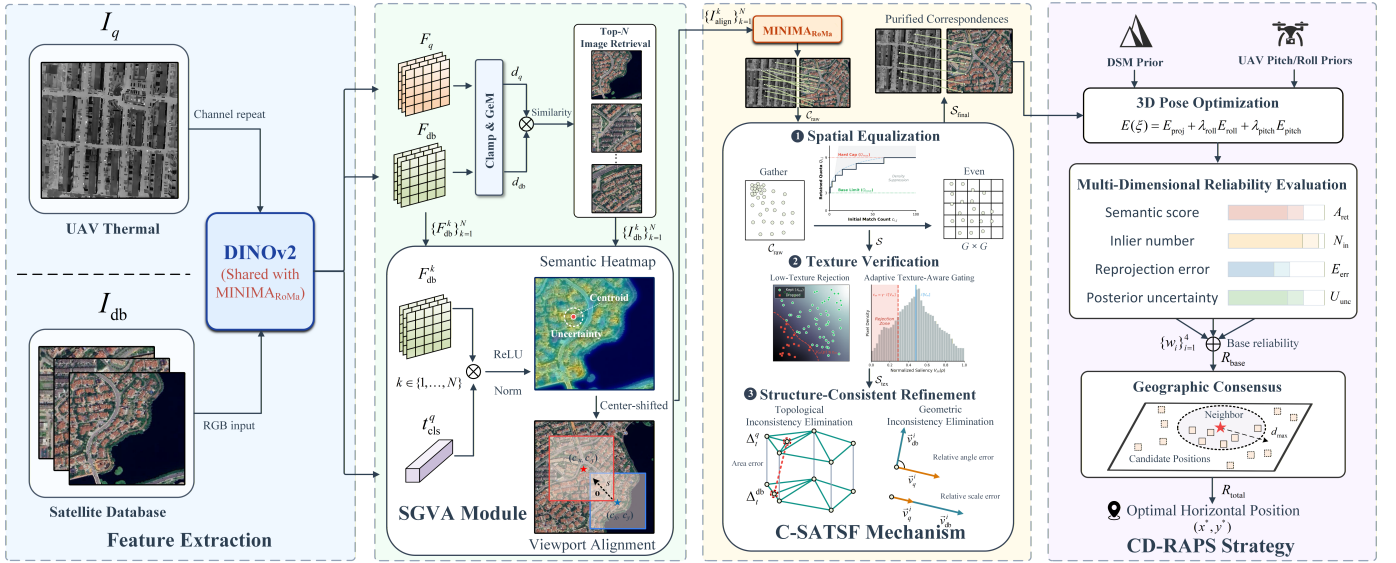


Fig. 2. Overview of the proposed SCC-Loc framework. The pipeline consists of four main stages: **(1) Feature Extraction:** A shared DINOv2 backbone bridges the thermal-visible modality gap to extract dense spatial features and global tokens; **(2) SGVA Module:** The Semantic-Guided Viewport Alignment module leverages the query’s global token to adaptively crop and align the retrieved satellite candidates with the UAV field-of-view; **(3) C-SATSF Mechanism:** Following dense matching via MINIMARoMa, the Cascaded Spatial-Adaptive Texture-Structure Filtering progressively purifies raw correspondences by eliminating spatial, textural, and structural inconsistencies; **(4) CD-RAPS Strategy:** The Consensus-Driven Reliability-Aware Position Selection integrates 3D pose optimization and multi-dimensional reliability evaluation to vote for the robust optimal horizontal position via geographic consensus.

critical data scarcity, we introduce **Thermal-UAV**, a comprehensive, multi-region, and multi-temporal thermal-satellite localization benchmark. Second, algorithmically, we propose **SCC-Loc**, a *training-free* framework that achieves exceptional zero-shot generalization. Instead of training cross-modal feature extractors from scratch, SCC-Loc adopts a coarse-to-fine two-stage strategy that elegantly integrates off-the-shelf visual retrieval and matching models. By designing bespoke intermediate modules to bridge these heterogeneous models, we construct a unified and seamless pipeline. Evaluated comprehensively on our Thermal-UAV dataset, SCC-Loc robustly overcomes the severe cross-modal gap without requiring a single epoch of domain-specific fine-tuning, setting a new paradigm for highly generalizable all-weather UAV navigation.

III. PROPOSED METHOD

A. Overview

As illustrated in Fig. 2, the SCC-Loc framework presents a cohesive coarse-to-fine paradigm. By sharing the DINOv2 [35] backbone of the MINIMARoMa [29] matcher across global retrieval and dense matching, it efficiently bridges the thermal-visible gap without redundant memory overhead. First, the Semantic-Guided Viewport Alignment (SGVA) module corrects spatial quantization bias by aligning the viewport center via the UAV’s global [CLS] token. Next, the aligned patches undergo dense matching, where the Cascaded Spatial-Adaptive Texture-Structure Filtering (C-SATSF) acts as a hierarchical sieve to distill dependable correspondences and reject massive cross-modal outliers. Finally, to evade the “low residual, high drift” trap induced by visual decoys, the Consensus-Driven Reliability-Aware Position Selection (CD-RAPS) utilizes physically constrained non-linear optimization, multi-

dimensional reliability evaluation, and geographic consensus to robustly deduce the final optimal position.

B. Semantic-Guided Viewport Alignment Module

To rectify the spatial misalignments between the Top- N retrieved satellite candidates and the field view of the thermal UAV image, we propose the SGVA module. This module directly exploits the high-level semantic activations extracted by the shared DINOv2 backbone to adaptively optimize the crop center and scale of the satellite tiles, thereby ensuring viewport alignment between the satellite imagery and the thermal query for the subsequent fine-grained matching.

Formally, the global retrieval process begins by feeding the thermal query I_q and the visible database images I_{db} into the shared DINOv2 backbone Φ_{DINOv2} to extract their corresponding dense feature maps, denoted as $F_q \in \mathbb{R}^{H \times W \times D}$ and $F_{db} \in \mathbb{R}^{H \times W \times D}$, respectively. To derive a compact global representation, we treat the dense feature map for each modality $m \in \{q, db\}$ as a set of spatial feature tokens \mathcal{X}_m , where the cardinality is $|\mathcal{X}_m| = H \times W$. These tokens are then aggregated via Generalized Mean (GeM) pooling [36] to obtain the modality-invariant global descriptor $d_m \in \mathbb{R}^D$:

$$d_m = \left(\frac{1}{|\mathcal{X}_m|} \sum_{x \in \mathcal{X}_m} \text{clamp}(x, \epsilon_{\min})^\psi \right)^{\frac{1}{\psi}}, \quad m \in \{q, db\}, \quad (1)$$

where $x \in \mathcal{X}_m$ represents an individual spatial token of dimension D . The pooling exponent ψ is configured as a fixed empirical constant, while $\text{clamp}(\cdot, \epsilon_{\min})$ enforces a lower bound ϵ_{\min} to discard negative and negligible activations, thereby physically directing the pooling mechanism to focus

on high-response regions. Following the L_2 -normalization of the resulting pooled descriptors d_q and d_{db} , we compute their cosine similarity and rank the database images to retrieve the top- N candidate set $\mathcal{R} = \{I_{db}^k\}_{k=1}^N$ [19].

Having obtained the coarse candidate set \mathcal{R} , we next establish a semantic interaction mechanism to dynamically align the viewport for each $I_{db}^k \in \mathcal{R}$. Diverging from the texture-oriented GeM features used in global retrieval, we leverage the [CLS] token $t_{cls}^q \in \mathbb{R}^D$ [37] extracted via Φ_{DINOv2} —which encapsulates the global semantic context of the UAV view—to interrogate the dense patch features $F_{db}^k \in \mathbb{R}^{H \times W \times D}$ of the k -th satellite candidate. This interaction generates a semantic correlation heatmap $M \in \mathbb{R}^{H \times W}$ via pixel-wise cosine similarity, providing precise spatial guidance for the subsequent adaptive cropping:

$$M_{i,j} = \langle \text{Norm}(t_{cls}^q), \text{Norm}(F_{db}^k[i, j]) \rangle, \quad (2)$$

where (i, j) denotes the spatial coordinates within the $H \times W$ feature map, $\text{Norm}(\cdot)$ denotes the L_2 -normalization operation, and $\langle \cdot, \cdot \rangle$ represents the dot product. This heatmap highlights regions in the satellite imagery that semantically align with the global view of the UAV.

To distill precise geometric cues from M , we interpret it as a probability distribution. Specifically, we apply ReLU rectification and normalization to obtain the spatial probability mass function \mathbf{P} :

$$\mathbf{P}_{i,j} = \frac{\text{ReLU}(M_{i,j})}{\sum_{u,v} \text{ReLU}(M_{u,v})}. \quad (3)$$

We then compute the center of gravity μ_{map} and the spatial standard deviation σ_{map} to estimate the target centroid and localization uncertainty, respectively:

$$\mu_{\text{map}} = \sum_{i,j} \mathbf{P}_{i,j} \cdot \mathbf{x}_{i,j}, \quad \sigma_{\text{map}} = \sqrt{\sum_{i,j} \mathbf{P}_{i,j} \cdot \|\mathbf{x}_{i,j} - \mu_{\text{map}}\|^2}, \quad (4)$$

where $\mathbf{x}_{i,j}$ represents the 2D normalized spatial coordinates corresponding to the grid index (i, j) .

Based on the estimated centroid μ_{map} and localization uncertainty σ_{map} , we introduce a dynamic modulation mechanism to derive the optimal crop parameters: the normalized center shift $\mathbf{o} = (o_x, o_y)$ and the elastic scale s . The complete adaptive parameter calculation is unified as follows:

$$\begin{cases} \eta = \lambda \cdot \sigma_{\text{map}}, \\ g = 1 + \alpha(1 - \eta), \\ s = 1 + \beta \cdot \eta, \\ \mathbf{o} = (\mu_{\text{map}} - 0.5) \cdot g, \end{cases} \quad (5)$$

where $\eta \in [0, 1]$ is the normalized uncertainty score scaled by a sensitivity hyperparameter λ . The variable g serves as an adaptive shifting gain, controlled by a confidence boost factor α . The parameter β dictates the expansion rate of the field of view for the elastic scale s . For the shift calculation, 0.5 represents the normalized center of the original satellite tile.

Subsequently, given the initial satellite retrieval patch with physical dimensions $w \times h$ and center (c_x, c_y) , the geometry of

Algorithm 1: Semantic-Guided Viewport Alignment Module

Input : UAV query semantics t_{cls}^q ; Satellite features F_{db}^k ; Candidate image I_{db}^k with center (c_x, c_y) and size (w, h) .

Output: Aligned satellite viewport I_{align}^k .

1 Part 1: Semantic Activation

2 $M \leftarrow \text{CosineSimilarity}(t_{cls}^q, F_{db}^k)$
 3 $\mathbf{P} \leftarrow \text{Normalize}(\text{ReLU}(M))$

4 Part 2: Parameter Calculation

5 $\mu_{\text{map}}, \sigma_{\text{map}} \leftarrow \text{EstimateDistribution}(\mathbf{P})$
 6 $\eta \leftarrow \lambda \cdot \sigma_{\text{map}}$
 7 $g \leftarrow 1 + \alpha(1 - \eta)$
 8 $s \leftarrow 1 + \beta \cdot \eta$
 9 $\mathbf{o} \leftarrow (\mu_{\text{map}} - 0.5) \cdot g$

10 Part 3: Viewport Alignment

11 $(c'_x, c'_y) \leftarrow (c_x, c_y) + \mathbf{o} \cdot (w, h)$
 12 $I_{align}^k \leftarrow \text{Crop}(I_{db}^k, c'_x, c'_y, s \cdot w, s \cdot h)$
 13 **return** I_{align}^k

the newly adapted crop—defined by its updated center (c'_x, c'_y) and dimensions (w', h') —is formulated:

$$\begin{aligned} c'_x &= c_x + o_x \cdot w, & w' &= s \cdot w, \\ c'_y &= c_y + o_y \cdot h, & h' &= s \cdot h. \end{aligned} \quad (6)$$

Intuitively, this coupled formulation ensures that low uncertainty ($\eta \rightarrow 0$) triggers a larger gain g to boldly shift the crop center towards the semantic peak μ . Conversely, high uncertainty ($\eta \rightarrow 1$) conservatively reduces the shifting step and explicitly enlarges the patch dimensions (w', h') to preserve a broader context.

Finally, based on these updated geometric parameters, we extract the adaptively aligned satellite viewport, denoted as I_{align}^k . This aligned patch I_{align}^k , along with the thermal UAV query I_q , are seamlessly forwarded to the MINIMA_{RoMa} model for fine-grained matching.

By explicitly resolving the spatial misalignments at the region level, our SGVA module provides a viewport alignment search region for MINIMA_{RoMa}. This enables the matcher to robustly establish dense cross-spectral correspondences, thereby completing a highly reliable coarse-to-fine localization pipeline.

The complete workflow of the SGVA module is shown in Algorithm 1.

C. Cascaded Spatial-Adaptive Texture-Structure Filtering Mechanism

To purify the dense tentative correspondences established by the MINIMA_{RoMa} matcher into a coherent set of highly reliable inliers, effectively suppressing the substantial outliers induced by severe cross-modal discrepancies, we propose the C-SATSF mechanism. C-SATSF functions as a hierarchical sieve, rigorously enforcing constraints through three progressive operations: spatial equalization, texture verification, and structure-consistent refinement.

Algorithm 2: Cascaded Spatial-Adaptive Texture-Structure Filtering Mechanism

Input : UAV Thermal Query I_q ; Aligned Satellite Viewport I_{align}^k .
Output: Highly dependable cross-modal inlier set $\mathcal{S}_{\text{final}}^{(k)}$.

- 1 $\mathcal{C}_{\text{raw}} \leftarrow \text{MINIMA}_{\text{RoMa}}(I_q, I_{\text{align}}^k)$
- 2 **Part 1: Density-Aware Spatial Equalization**
- 3 $\mathcal{Q} \leftarrow \text{ComputeLogQuotas}(\mathcal{C}_{\text{raw}})$
- 4 $\mathcal{S} \leftarrow \text{SpatialEqualize}(\mathcal{C}_{\text{raw}}, \mathcal{Q})$
- 5 **Part 2: Adaptive Texture Saliency Verification**
- 6 $V_q, V_{\text{db}} \leftarrow \text{ComputeLocalSaliency}(\mathcal{S})$
- 7 $\epsilon_q, \epsilon_{\text{db}} \leftarrow \gamma \cdot \mathbb{E}[V_q], \gamma \cdot \mathbb{E}[V_{\text{db}}]$
- 8 $\mathcal{S}_{\text{tex}} \leftarrow \{(p_q, p_{\text{db}}) \in \mathcal{S} \mid V_q(p_q) > \epsilon_q \wedge V_{\text{db}}(p_{\text{db}}) > \epsilon_{\text{db}}\}$
- 9 **Part 3: Structure-Consistent Geometric Refinement**
- 10 $\kappa(p_q) \leftarrow \text{ComputeNegativeVoteRate}(\mathcal{S}_{\text{tex}})$
- 11 $\mathcal{S}_{\text{topo}} \leftarrow \{(p_q, p_{\text{db}}) \in \mathcal{S}_{\text{tex}} \mid \kappa(p_q) \leq 0.5\}$
- 12 $\mathcal{S}_{\text{final}}^{(k)} \leftarrow \text{EnforceGlobalConsistency}(\mathcal{S}_{\text{topo}}, \epsilon_{\text{ang}}, \epsilon_{\text{scale}})$
- 13 **return** $\mathcal{S}_{\text{final}}^{(k)}$

1) Density-Aware Spatial Equalization: Conventional confidence-based filtering tends to cluster keypoints in high-contrast regions (e.g., isolated prominent structures) while neglecting sparse but geometrically critical areas. This uneven spatial distribution leads to ill-conditioned configurations for the subsequent PnP solver [38].

To counteract this, we employ a grid-based regularization with a logarithmic dynamic quota. We partition the image domain into a $G \times G$ grid. For each cell (i, j) , instead of enforcing a rigid capacity, we retain a dynamic number of matches $Q_{i,j}$ derived from the local feature density. Given the initial raw match set \mathcal{C}_{raw} , let $\mathcal{C}_{i,j}$ denote the subset of raw matches falling within cell (i, j) , and $c_{i,j} = |\mathcal{C}_{i,j}|$ be its cardinality. The dynamic quota and the spatially equalized output set \mathcal{S} are jointly formulated as:

$$\begin{cases} Q_{i,j} = \min(Q_{\text{base}} + \lfloor \log_2(c_{i,j} + 1) \rfloor, Q_{\text{max}}), \\ \mathcal{S} = \bigcup_{i,j=1}^G \text{TopK}(\mathcal{C}_{i,j}, Q_{i,j}), \end{cases} \quad (7)$$

where Q_{base} is the minimum reservation limit, Q_{max} is the absolute upper bound (empirically set to $3Q_{\text{base}}$), $\lfloor \cdot \rfloor$ denotes the floor operation, $\text{TopK}(\cdot, n)$ extracts the top n matches based on their initial confidence scores, and $\bigcup_{i,j=1}^G$ denotes the set union across all $G \times G$ spatial cells.

This logarithmic growth ensures that texture-rich regions contribute marginally more high-quality points to leverage their reliability, while the hard cap Q_{max} prevents them from dominating the global distribution. This guarantees a uniform and well-conditioned spatial coverage, yielding a robust initial set \mathcal{S} for the subsequent texture verification stage.

2) Adaptive Texture Saliency Verification: Following spatial equalization, we address the matching ambiguity prevalent in

texture-less regions—a challenge fundamentally exacerbated by the modality gap between UAV thermal imagery (which often exhibits low contrast) and visible satellite imagery (which provides abundant high-frequency details).

We first compute a local saliency map V_m for each modality $m \in \{q, \text{db}\}$ to quantify texture richness. For a given keypoint p , let $\mathcal{W}(p)$ denote its spatial neighborhood. The local variance $\sigma_m^2(p)$ within $\mathcal{W}(p)$ and the subsequent normalized local saliency $V_m(p)$ are jointly formulated as:

$$\begin{cases} \sigma_m^2(p) = \mathbb{E}[I_m^2(p)] - (\mathbb{E}[I_m(p)])^2, \\ V_m(p) = \frac{\sigma_m(p) - \sigma_m^{\min}}{\sigma_m^{\max} - \sigma_m^{\min}}, \end{cases} \quad (8)$$

where $\mathbb{E}[\cdot]$ denotes the expectation operator, $I_m(p)$ represents the normalized image intensity, and σ_m^{\min} and σ_m^{\max} denote the global minimum and maximum standard deviations across the respective modality. This effectively maps the local texture richness to a unified saliency scale $V_m(p) \in [0, 1]$.

To actively reject unreliable matches in feature-poor areas (e.g., large water bodies), we establish an adaptive saliency threshold ϵ_m for each modality. Given the spatially equalized match set \mathcal{S} consisting of corresponding keypoint pairs (p_q, p_{db}) , the texture-aware gating mechanism formulates this threshold and outputs a purified subset \mathcal{S}_{tex} as follows:

$$\begin{cases} \epsilon_m = \gamma \cdot \mathbb{E}[V_m], \quad m \in \{q, \text{db}\}, \\ \mathcal{S}_{\text{tex}} = \{(p_q, p_{\text{db}}) \in \mathcal{S} \mid V_q(p_q) > \epsilon_q \wedge V_{\text{db}}(p_{\text{db}}) > \epsilon_{\text{db}}\}, \end{cases} \quad (9)$$

where γ is a threshold scaling factor, and \wedge denotes the logical AND operator, strictly requiring a match to surpass the adaptive saliency lower bound in both modalities simultaneously. By effectively pruning low-texture ambiguous matching pairs, this filtering layer significantly reduces the outlier ratio, ensuring that only correspondences anchored on salient physical structures are forwarded to the subsequent geometric refinement stage.

3) Structure-Consistent Geometric Refinement: Following texture saliency verification, the surviving correspondences may still contain spatially erroneous outliers caused by semantically similar but repetitive patterns (e.g., identical rooftops). To eliminate these structural outliers, this final geometric refinement stage enforces structural consistency by unifying local topological invariance and global geometric rigidity.

We leverage Delaunay Triangulation on the UAV keypoints to capture the local spatial graph [39], [40]. Assuming the transformation between the UAV view and the satellite ortho-photo locally approximates a similarity transformation, the area ratio of corresponding triangles across modalities should remain invariant. Let Δ_t^q and Δ_t^{db} denote the t -th corresponding triangle pair in the query and database images, respectively. The cross-modal area ratio ρ_t and the subsequent topological deviation δ_t relative to the global consensus are formulated as:

$$\begin{cases} \rho_t = \frac{\text{Area}(\Delta_t^{\text{db}})}{\text{Area}(\Delta_t^q)}, \\ \delta_t = \frac{|\rho_t - \text{med}(\boldsymbol{\rho})|}{\text{med}(\boldsymbol{\rho})}, \end{cases} \quad (10)$$

where $\text{Area}(\cdot)$ computes the geometric area of a given triangle, ρ denotes the set of all triangle area ratios, and $\text{med}(\cdot)$ represents the robust median operator.

To gracefully handle local distortions, we deploy a local voting mechanism on the texture-filtered set \mathcal{S}_{tex} . Let $\mathcal{T}(p_q)$ denote the local neighborhood set of triangles sharing the query keypoint p_q , and $\Delta_t^q \in \mathcal{T}(p_q)$ represent the t -th connected triangle in the UAV thermal view. A triangle is penalized if its topological deviation δ_t exceeds a topological tolerance threshold ϵ_{topo} . The negative vote rate $\kappa(p_q)$ and the resulting topologically purified subset $\mathcal{S}_{\text{topo}}$ are sequentially formulated as:

$$\begin{cases} \kappa(p_q) = \frac{1}{|\mathcal{T}(p_q)|} \sum_{\Delta_t^q \in \mathcal{T}(p_q)} \mathbb{I}(\delta_t > \epsilon_{\text{topo}}), \\ \mathcal{S}_{\text{topo}} = \{(p_q, p_{\text{db}}) \in \mathcal{S}_{\text{tex}} \mid \kappa(p_q) \leq 0.5\}, \end{cases} \quad (11)$$

where $\mathbb{I}(\cdot)$ denotes the indicator function, and $|\mathcal{T}(p_q)|$ is the total number of adjacent triangles for p_q . Matches exhibiting a negative vote rate greater than 50% are classified as topological anomalies and strictly eradicated from the candidate pool.

Complementarily, we enforce global consistency in scale and orientation on the surviving set $\mathcal{S}_{\text{topo}}$ to prevent structural collapse. Let \bar{p}_q and \bar{p}_{db} denote the geometric centroids of the keypoints in $\mathcal{S}_{\text{topo}}$ for the query and database modalities, respectively. We define the heading vectors \vec{v}_q^i and \vec{v}_{db}^i for the i -th keypoint pair $(p_q^i, p_{\text{db}}^i) \in \mathcal{S}_{\text{topo}}$, alongside the relative rotation ϕ_i , as:

$$\begin{aligned} \vec{v}_q^i &= p_q^i - \bar{p}_q, & \vec{v}_{\text{db}}^i &= p_{\text{db}}^i - \bar{p}_{\text{db}}, \\ \phi_i &= \text{ang}(\vec{v}_{\text{db}}^i) - \text{ang}(\vec{v}_q^i), \end{aligned} \quad (12)$$

where $\text{ang}(\cdot)$ denotes the polar angle of a given 2D vector. A match is strictly validated only if it satisfies the global consensus constraints on both rotation and scale simultaneously. The final highly purified matching set $\mathcal{S}_{\text{final}}$ is extracted as:

$$\mathcal{S}_{\text{final}} = \left\{ (p_q^i, p_{\text{db}}^i) \in \mathcal{S}_{\text{topo}} \mid \begin{aligned} &|\phi_i - \text{med}(\phi)| < \epsilon_{\text{ang}} \\ &\wedge \left| \frac{\|\vec{v}_{\text{db}}^i\|}{\bar{s} \cdot \|\vec{v}_q^i\|} - 1 \right| \leq \epsilon_{\text{scale}} \end{aligned} \right\}, \quad (13)$$

where ϕ is the set of relative rotations, \bar{s} is the median scale, and ϵ_{ang} and ϵ_{scale} are the corresponding tolerance thresholds.

By coupling local topological invariance with global geometric rigidity, this final filtering layer systematically eradicates spatially misplaced outliers that share similar visual semantics.

In summary, the proposed C-SATSF module functions as a hierarchical gating mechanism that synergizes spatial equalization, texture verification, and structure-consistent refinement. By progressively filtering out spatial imbalances, texture ambiguities, and structural anomalies, it distills raw matches into a highly reliable consensus set $\mathcal{S}_{\text{final}}$, laying a solid foundation for the subsequent pose solver.

The complete workflow of the C-SATSF mechanism is shown in Algorithm 2.

D. Consensus-Driven Reliability-Aware Position Selection Strategy

To identify the optimal geographic position from the Top- N candidates and suppress visual decoys, we propose the CD-RAPS strategy. In large-scale search spaces, global structural repetition often yields deceptively high PnP inliers for completely incorrect poses [41]. To overcome this, CD-RAPS progressively refines candidate poses via physically constrained optimization, evaluates their multi-dimensional reliability, and pinpoints the true location through geographic consensus voting.

For a given candidate k , building upon the highly dependable 2D-2D correspondence set $\mathcal{S}_{\text{final}}^{(k)}$ preserved by the preceding filtering module, let $(p_q^i, p_{\text{db}}^i) \in \mathcal{S}_{\text{final}}^{(k)}$ denote the i -th matched keypoint pair. By extracting the elevation prior from a DSM at the satellite 2D location p_{db}^i , we lift it to the 3D geographic coordinate \mathbf{P}_i . This forms the 2D-3D correspondence set $\mathcal{P} = \{(p_q^i, \mathbf{P}_i)\}$, from which an initial PnP pose is computed [9]. Instead of directly utilizing this initial solution, we formulate a non-linear optimization guided by physical UAV flight priors [42]. For notational clarity, we omit the candidate index k in the subsequent single-pose derivation.

Considering that UAVs in orthographic observation tasks typically employ three-axis stabilized gimbals, the camera's roll angle is physically constrained near zero. We incorporate this hardware-induced limitation, alongside the flight telemetry pitch prior, directly into the optimization objective. This explicitly prevents the solver from converging to physically impossible configurations, thereby guaranteeing the geometric correctness of the estimated pose.

To implement these physical constraints mathematically, let the camera state be parameterized by $\boldsymbol{\xi} \in \mathfrak{se}(3)$, corresponding to the Lie algebra of the Special Euclidean group $SE(3)$ [43]. This serves as a minimal and singularity-free parameterization for continuous optimization, where the corresponding rotation matrix $\mathbf{R}_{\text{wc}}(\boldsymbol{\xi})$ and translation vector $\mathbf{t}_{\text{wc}}(\boldsymbol{\xi})$ are iteratively recovered via the exponential map. Specifically, the optimal pose parameter $\boldsymbol{\xi}$ is obtained by minimizing the joint objective function $E(\boldsymbol{\xi})$:

$$\begin{aligned} E(\boldsymbol{\xi}) &= \sum_{(p_q^i, \mathbf{P}_i) \in \mathcal{P}_{\text{in}}} \left\| p_q^i - \pi(\mathbf{P}_i, \boldsymbol{\xi}) \right\|^2 + \lambda_{\text{roll}} \left((\mathbf{R}_{\text{wc}}(\boldsymbol{\xi}) \mathbf{e}_1)^\top \mathbf{n}_z \right)^2 \\ &\quad + \lambda_{\text{pitch}} \left(\theta_{\text{pitch}}(\boldsymbol{\xi}) - \theta_{\text{prior}} \right)^2, \end{aligned} \quad (14)$$

where $\mathcal{P}_{\text{in}} \subseteq \mathcal{P}$ denotes the robust inlier subset identified during the initial PnP computation, and $\pi(\cdot)$ represents the camera projection function. For the attitude constraints, $\mathbf{e}_1 = [1, 0, 0]^\top$ and $\mathbf{n}_z = [0, 0, 1]^\top$ refer to the camera's lateral axis and the world gravity vector, respectively. The term $\theta_{\text{pitch}}(\boldsymbol{\xi})$ represents the pitch angle analytically derived from the current pose state $\boldsymbol{\xi}$ at each optimization iteration, θ_{prior} is the constant pitch angle prior acquired from the UAV's flight telemetry, and λ_{roll} and λ_{pitch} act as adaptive weighting multipliers.

Furthermore, upon convergence of the optimization, we rigorously quantify the geometric positional uncertainty U_{unc} by capturing the local curvature of the objective landscape. Let \mathbf{J} denote the Jacobian matrix evaluated at the optimal solution.

We approximate the Fisher Information Matrix as $\mathbf{H} \approx \mathbf{J}^\top \mathbf{J}$. Subsequently, the posterior covariance matrix Σ_ξ of the pose parameters and the uncertainty metric U_{unc} are derived via the Cramér-Rao Lower Bound [44]:

$$\Sigma_\xi = \hat{\sigma}^2 \mathbf{H}^{-1}, \quad U_{\text{unc}} = \sqrt{\text{Tr}(\Sigma_{\text{pos}})}, \quad (15)$$

where $\hat{\sigma}^2$ denotes the posterior residual variance, Σ_{pos} represents the 3×3 translational sub-matrix extracted from the full covariance Σ_ξ , and $\text{Tr}(\cdot)$ signifies the matrix trace operator. To ensure dimensional consistency, U_{unc} compresses the multidimensional estimation error into a scalar metric representing the positional standard deviation. Physically, a high U_{unc} reveals a flat objective landscape indicative of unstable solutions (e.g., caused by thermal image blur and low contrast), whereas a low value signifies a sharp, well-constrained minimum.

To preserve the statistical integrity of the candidate pool, a hard gating mechanism automatically rejects candidates that fail to yield a convergent solution, possess insufficient inliers, or exhibit mathematically singular Hessian matrices that result in infinite uncertainty [45].

For the surviving candidates, we evaluate their reliability across four dimensions: the semantic cosine similarity A_{ret} , the post-optimization inlier count N_{in} , the reprojection error E_{err} , and the geometric uncertainty U_{unc} . To ensure scale consistency, these metrics are Min-Max normalized to $[0, 1]$. By inverting the error-based metrics (E_{err} and U_{unc}), we align all indicators such that higher values denote greater reliability. Ultimately, the base reliability $R_{\text{base}}^{(k)}$ for the k -th candidate is aggregated via weighted fusion:

$$R_{\text{base}}^{(k)} = w_1 A_{\text{ret}}^{(k)} + w_2 N_{\text{in}}^{(k)} + w_3 E_{\text{err}}^{(k)} + w_4 U_{\text{unc}}^{(k)}, \quad (16)$$

where $\{w_i\}_{i=1}^4$ are empirically determined non-negative weights satisfying $\sum_{i=1}^4 w_i = 1$.

Finally, to exploit the geographic consensus that correct candidates cluster tightly while incorrect visual decoys scatter randomly, we introduce a distance-decaying spatial consistency voting mechanism. For a valid candidate k located at geographic coordinate \mathbf{L}_k , its spatial neighborhood \mathcal{N}_k comprises the nearest candidates within a specific geographic distance threshold d_{max} . Candidates within this radius contribute a weighted geographic consensus score $C_{\text{geo}}^{(k)}$ to candidate k , penalizing distant neighbors linearly:

$$C_{\text{geo}}^{(k)} = \sum_{j \in \mathcal{N}_k, R_{\text{base}}^{(j)} \geq \tau} R_{\text{base}}^{(j)} \cdot \left(1 - \frac{\|\mathbf{L}_k - \mathbf{L}_j\|_2}{d_{\text{max}}}\right), \quad (17)$$

where τ denotes the minimum reliability threshold that exclusively accepts contributions from high-confidence neighbors, effectively preventing score accumulation from low-quality outliers. Subsequently, the total reliability score $R_{\text{total}}^{(k)}$ for each candidate is formulated by fusing the base reliability with the geographic consensus reward:

$$R_{\text{total}}^{(k)} = R_{\text{base}}^{(k)} + \min\left(\omega_{\text{geo}} C_{\text{geo}}^{(k)}, \omega_{\text{base}} R_{\text{base}}^{(k)}\right), \quad (18)$$

where ω_{geo} and ω_{base} are scaling factors controlling the consensus reward. Ultimately, the final optimal position index k^* is

Algorithm 3: Consensus-Driven Reliability-Aware Position Selection Strategy

Input : Top- N inlier sets $\{\mathcal{S}_{\text{final}}^{(k)}\}_{k=1}^N$ and retrieval scores $\{A_{\text{ret}}^{(k)}\}_{k=1}^N$; Aligned DSM Database \mathcal{D}_{DSM} .

Output: Optimal Absolute Horizontal Position (x^*, y^*) .

1 Part 1: Physically Constrained Pose Optimization
2 for $k = 1$ **to** N **do**

 3 $\mathcal{P} \leftarrow \text{LiftTo3D}(\mathcal{S}_{\text{final}}^{(k)}, \mathcal{D}_{\text{DSM}})$

 4 $\xi_{\text{init}}, \mathcal{P}_{\text{in}} \leftarrow \text{ComputeInitialPnP}(\mathcal{P})$

 5 $N_{\text{in}}^{(k)} \leftarrow |\mathcal{P}_{\text{in}}|$

 6 $\xi_k \leftarrow \arg \min_{\xi} E(\xi | \xi_{\text{init}})$

 7 $E_{\text{err}}^{(k)} \leftarrow E(\xi_k)$

 8 $U_{\text{unc}}^{(k)} \leftarrow \sqrt{\text{Tr}\left([\hat{\sigma}^2 \mathbf{H}(\xi_k)^{-1}]_{\text{pos}}\right)}$

 9 $\mathbf{L}_k \leftarrow \mathbf{t}_{\text{wc}}(\xi_k)$

 10 $R_{\text{base}}^{(k)} \leftarrow \text{BaseReliability}(A_{\text{ret}}^{(k)}, N_{\text{in}}^{(k)}, E_{\text{err}}^{(k)}, U_{\text{unc}}^{(k)})$
11 end
12 Part 2: Geographic Consensus Voting
13 for $k = 1$ **to** N **do**

 14 $C_{\text{geo}}^{(k)} \leftarrow \sum_{j \in \mathcal{N}_k | R_{\text{base}}^{(j)} \geq \tau} R_{\text{base}}^{(j)} \cdot \left(1 - \frac{\|\mathbf{L}_k - \mathbf{L}_j\|_2}{d_{\text{max}}}\right)$

 15 $R_{\text{total}}^{(k)} \leftarrow R_{\text{base}}^{(k)} + \min(\omega_{\text{geo}} C_{\text{geo}}^{(k)}, \omega_{\text{base}} R_{\text{base}}^{(k)})$
16 end
17 Part 3: Optimal Selection

 18 $k^* \leftarrow \arg \max_k R_{\text{total}}^{(k)}$

 19 $(x^*, y^*) \leftarrow \mathbf{L}_{k^*}$
20 return (x^*, y^*)

robustly determined by selecting the candidate with the highest total reliability score. The final UAV horizontal position (x^*, y^*) is then explicitly retrieved from the pre-computed spatial location \mathbf{L}_{k^*} of this selected optimal candidate.

Through this comprehensive synergy of physically constrained optimization, multi-dimensional reliability evaluation, and geographic consensus, the proposed CD-RAPS strategy effectively eradicates visual decoys, thereby completing a highly accurate and robust UAV geo-localization pipeline.

The complete workflow of the CD-RAPS strategy is shown in Algorithm 3.

IV. EXPERIMENTAL SETUP

A. Datasets

To address the critical scarcity of large-scale benchmarks for cross-modal UAV geo-localization, we construct the Thermal-UAV dataset, a comprehensive benchmark comprising 11,890 thermal images collected using a DJI Matrice 4T drone¹ at varying altitudes ranging from 300 m to 350 m (nadir view). Specifically, the data acquisition spans multiple time periods (daytime and nighttime) across highly complex urban and rural

¹<https://www.dji.com/support/product/>

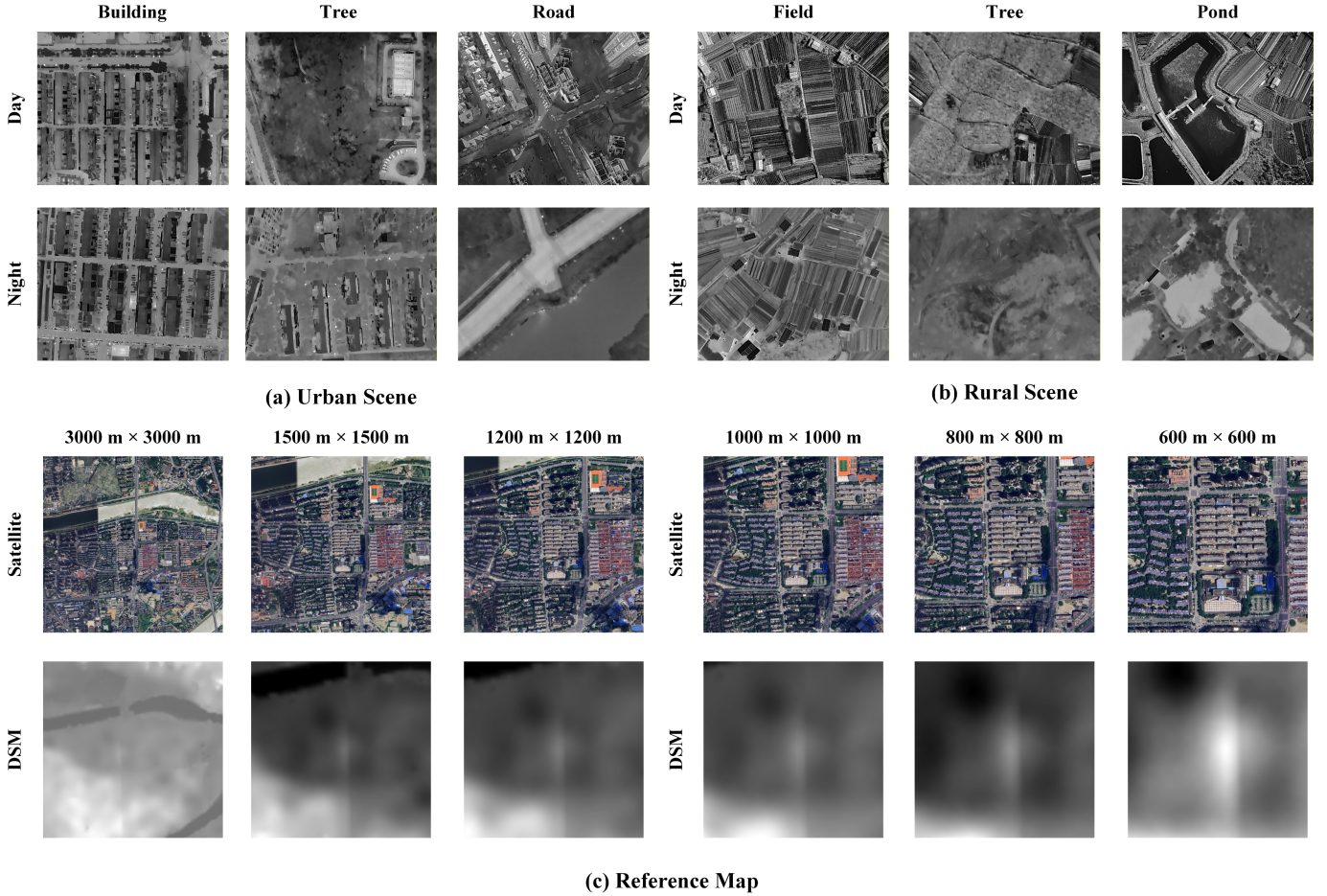


Fig. 3. Visual samples from the constructed Thermal-UAV dataset. The dataset systematically captures profound modality discrepancies and diurnal thermal variations across diverse spatial topologies: (a) Urban and (b) Rural Scenes showcase thermal UAV queries of distinct semantic categories (e.g., buildings, roads, fields) during daytime and nighttime; (c) Reference Map presents the global database at varying search scales, comprising visible-light satellite orthophotos and their spatially aligned Digital Surface Models (DSM) to supply crucial 3D elevation priors.

scenarios, explicitly designed to systematically capture diurnal thermal variations and diverse spatial topologies. As illustrated in Fig. 3(a) and (b), these representative thermal queries explicitly showcase the profound thermal-visible modality gap under distinct environmental conditions. The dataset is meticulously structured into dense, multi-segment flight trajectories, which is partitioned into training (8,115), validation (1,425), and testing (2,350) sets. The global reference database is constructed as a single, continuous large-scale map, comprising Google Earth satellite imagery² (0.26 m/pixel) paired with a spatially aligned DSM (5.29 m/pixel). Furthermore, Fig. 3(c) provides detailed visualizations of this unified reference map and explicitly illustrates the retrieval scenarios under varying search space sizes.

We evaluate our purely training-free SCC-Loc framework exclusively on the 2,350 test images. To ensure a fair comparison, we utilize the dataset’s training set to train the supervised domain-specific baseline models. We note that we do not evaluate our method on the existing Boson-nighttime dataset. This is because Boson-nighttime lacks essential topographic metadata—spatially aligned DSM—which are mandatory pre-

requisites for solving the absolute pose via 2D-3D PnP. Therefore, Thermal-UAV currently serves as the only comprehensive benchmark capable of evaluating such 3D-aware cross-modal pipelines.

B. Evaluation Metrics

We evaluate SCC-Loc across two stages: coarse retrieval and fine-grained localization. For coarse retrieval, we use **Recall@N** ($N \in \{3, 5, 10\}$) [6]. A retrieval is deemed a hit if the Position Deviation Error (PDE)—the normalized Euclidean distance between the retrieved patch center and the ground truth—is strictly less than 0.5 [9].

For fine-grained absolute position estimation, we measure geometric precision using **Acc@R** ($R \in \{5, 10, 20\}$) and **ME ± SD** [46]. **Acc@R** represents the percentage of predicted coordinates falling strictly within R meters of the ground truth. Additionally, we report the Mean Error (ME) and Standard Deviation (SD) in meters to quantify the overall metric accuracy and spatial robustness, respectively.

Finally, to assess deployment feasibility, we report the average **Inference Time** (seconds/query) and peak GPU **Memory Consumption** (MB) [47]. Specifically, the memory metric

²<https://www.google.com/maps>

strictly accounts for the model’s parameter footprint and inference overhead, explicitly excluding the reference database and data loading memory.

C. Baseline Methods

To evaluate SCC-Loc against the thermal-visible modality gap, we construct comprehensive baselines across three categories. First, for **coarse retrieval**, we employ CAMP [21] (visible-only trained) to assess zero-shot degradation, alongside foundation models DINOv2 [35] and DINOv3 [24] to test their inherent modality-invariant semantics. Second, for **fine-grained matching**, we couple these retrievers with varying feature matchers: RoMa [28] (an intra-modal dense matcher) to establish a baseline for performance degradation under severe spectral discrepancies; XoFTR [11], a fast semi-dense matcher inherently tailored for cross-modal association; and MINIMA_{RoMa} [29], which explicitly fine-tunes RoMa on a cross-modal benchmark to serve as a domain-adapted upper bound. Finally, we benchmark against **domain-specific networks** STHN [6] and NIVnet [34]. For fairness, both are retrained on our Thermal-UAV training split. Despite relying on planar homography regression rather than our zero-shot 3D-aware formulation, they provide a strong context for state-of-the-art supervised thermal-to-visible localization.

D. Implementation Details

Implementation Platform. We implement SCC-Loc in PyTorch, executing all experiments on a workstation equipped with an Intel Core i5-14600K CPU and an NVIDIA RTX 4060 Ti GPU.

Geo-Spatial Preprocessing. Assuming the UAV’s altitude, pitch, and yaw are available as onboard priors, we utilize the yaw prior to rotationally align the thermal queries with the North-oriented satellite maps. This eliminates large in-plane rotations, facilitating robust cross-modal retrieval. To maintain scale consistency, satellite patches are dynamically cropped based on the Ground Sampling Distance (GSD) [9]. We multiply the theoretical GSD by an empirical scaling factor s_{gsd} to enlarge the receptive field, providing richer peripheral context for subsequent fine-matching stages.

Hyperparameter Settings. For coarse retrieval, the continuous satellite ortho-photo is discretized into a searchable patch database using a sliding window with an overlap ratio ρ_{overlap} within a geographic search area A_{search} . To ensure full reproducibility, all hyperparameters governing the entire pipeline are detailed in Table I. Unless otherwise specified, these default settings remain strictly constant across all evaluations.

V. RESULTS

A. Illustrative Operation

To illustrate the internal workings of the SCC-Loc framework, Fig. 4 visualizes the stage-by-stage localization process across two challenging cross-modal scenarios (Urban and Rural). For each scenario, the UAV query is evaluated against an 800×800 m satellite reference area (with the GSD scaling

TABLE I
DETAILED HYPERPARAMETER CONFIGURATIONS FOR THE PROPOSED
SCC-LOC FRAMEWORK.

Hyperparameter Description	Symbol	Value
Coarse Retrieval Phase		
Geographic search area	A_{search}	$600 \times 600 \text{ m}^2$
Sliding window overlap	ρ_{overlap}	60%
GSD scaling factor	s_{gsd}	1.5
Minimum error tolerance	ϵ_{min}	10^{-6}
Pooling exponent	ψ	4
Semantic-Guided Viewport Alignment (SGVA)		
Sensitivity factor	λ	5.0
Confidence boost	α	0.5
Expansion rate	β	0.2
Cascaded Filtering Mechanism (C-SATSF)		
Grid partition size	G	8×8
Min. reservation limit	Q_{base}	3
Saliency threshold scalar	γ	0.5
Topological tolerance	ϵ_{topo}	0.4
Angular tolerance	ϵ_{ang}	20°
Scale tolerance	ϵ_{scale}	0.3
Consensus-Driven Selection (CD-RAPS)		
Roll constraint weight	λ_{roll}	1000
Pitch constraint weight	λ_{pitch}	15
Reliability weights	$\{w_i\}_{i=1}^4$	{0.1, 0.2, 0.35, 0.35}
Max. geographic distance	d_{max}	20 m
Min. reliability threshold	τ	0.3
Geo-consensus weight	ω_{geo}	0.2
Base reliability weight	ω_{base}	0.5

factor set to 1), tracking the evolution of the Top-3 retrieved candidates.

1) Adaptive Viewport and Dense Matching: Initially, inherent spatial quantization bias often marginalizes the target. As shown in the **Re-Cropping** columns, our SGVA module adaptively aligns the viewport, reducing the PDE (e.g., from 0.464 to 0.448 for the Top-3 urban candidate) to optimally bound the target. During the **Matching** stage, raw dense correspondences are established by MINIMA_{RoMa}. Our C-SATSF mechanism then acts as a rigorous geometric filter, preserving valid inliers (green lines) while robustly suppressing outlier matches on highly deceptive backgrounds.

2) Eradicating Decoys via Geographic Consensus: The core mechanism is explicitly revealed by contrasting the **Base score** with the **Final score** during **Localization**. Repetitive topologies (e.g., identical residential rooftops in Fig. 4(a) or similar agricultural plots in Fig. 4(b)) act as visual decoys. These decoys may acquire moderate base scores through raw feature similarity. However, because false candidates scatter randomly across the vast reference map, they fail to form a local geographic consensus. Consequently, they receive zero consensus reward, leaving their Final score strictly identical to their Base score (e.g., Row 1 in both scenarios).

Conversely, true geographic hypotheses inherently cluster. In the Rural Scene (Fig. 4(b)), the correct top candidates (Row

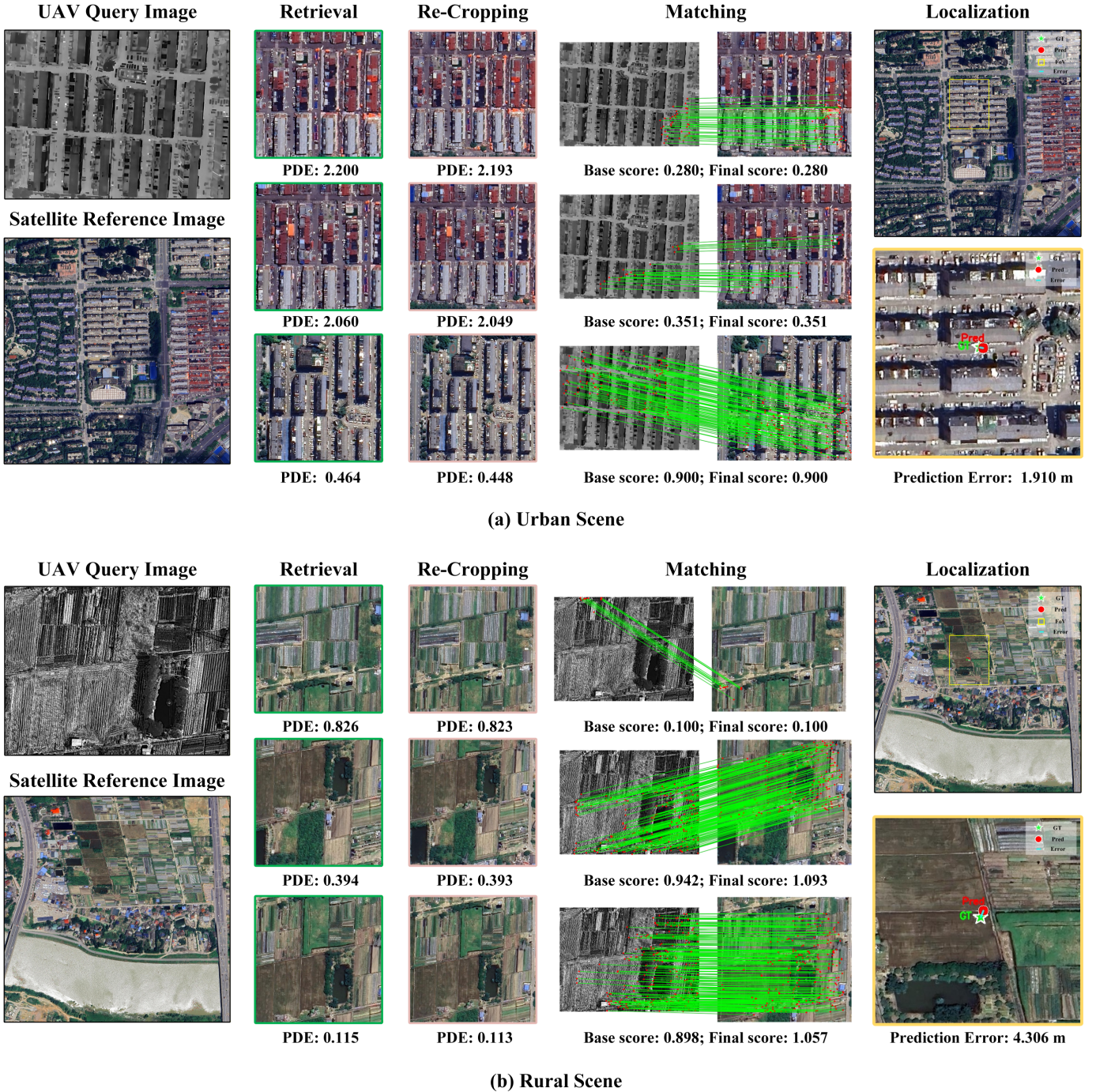


Fig. 4. Qualitative visualization of the proposed SCC-Loc pipeline in (a) Urban and (b) Rural scenarios. The process illustrates the adaptive correction of spatial quantization bias via the SGVA module (**Re-Cropping**) and the progressive elimination of structural outliers using the C-SATSF mechanism (**Matching**). Finally, based on the highly purified correspondences, the CD-RAPS strategy refines candidate poses via physically constrained optimization, and computes the total reliability (**Final score**) by fusing the multi-dimensional evaluation (**Base score**) with geographic consensus to determine the robust optimal hypothesis for precise **Localization**.

2 and Row 3) are spatially adjacent. Through the CD-RAPS strategy, they geographically validate each other, accumulating consensus votes that significantly boost their Final scores above their Base scores (e.g., surging from 0.898 to 1.057). This spatial voting mechanism effectively isolates and discards decoys, empowering SCC-Loc to robustly pinpoint the optimal location (yielding precise prediction errors of merely 1.910 m

and 4.306 m, respectively).

B. Comparison with Two-Stage Baselines

To comprehensively evaluate the effectiveness of the proposed SCC-Loc, we benchmark its Top-3, Top-5, and Top-10 retrieval performance against systematically composed two-stage baselines, as detailed in Table II. The quantitative results

TABLE II

QUANTITATIVE COMPARISON OF THE PROPOSED SCC-LOC FRAMEWORK AGAINST VARIOUS TWO-STAGE BASELINES, WHICH COMPRISE DIFFERENT COMBINATIONS OF RETRIEVAL AND MATCHING MODELS. THE BEST RESULTS ARE HIGHLIGHTED IN **BOLD**.

Method	Top-3 Candidates				Top-5 Candidates				Top-10 Candidates			
	Recall@3	Acc@5/10/20	ME \pm SD	Time	Recall@5	Acc@5/10/20	ME \pm SD	Time	Recall@10	Acc@5/10/20	ME \pm SD	Time
CAMP + XoFTR	75.15	1.53 / 5.96 / 16.51	280.52 \pm 374.93	1.03	85.70	1.66 / 6.94 / 20.04	193.75 \pm 306.82	1.24	96.13	1.66 / 8.13 / 23.79	121.00 \pm 216.86	1.79
CAMP + RoMa	75.15	3.06 / 12.04 / 31.49	91.89 \pm 139.31	4.01	85.70	4.26 / 14.00 / 36.98	69.00 \pm 105.93	6.30	96.13	4.38 / 15.83 / 39.70	49.17 \pm 82.95	11.97
CAMP + MINIMA _{RoMa}	75.15	4.72 / 15.57 / 40.43	84.26 \pm 131.58	4.22	85.70	4.77 / 17.62 / 46.17	61.79 \pm 111.69	6.60	96.13	6.77 / 21.11 / 49.83	40.92 \pm 78.34	12.53
DINOV2 + XoFTR	91.23	1.66 / 7.57 / 21.45	185.70 \pm 307.10	0.92	96.77	2.17 / 8.64 / 24.51	141.61 \pm 254.98	1.30	99.45	2.30 / 9.57 / 25.87	100.86 \pm 188.14	1.96
DINOV2 + RoMa	91.23	3.57 / 14.98 / 39.28	55.21 \pm 81.07	4.28	96.77	4.09 / 16.81 / 43.45	48.04 \pm 70.72	6.36	99.45	4.89 / 16.85 / 42.21	40.50 \pm 56.01	12.02
DINOV2 + MINIMA _{RoMa}	91.23	5.62 / 19.83 / 50.04	52.17 \pm 95.75	4.21	96.77	6.09 / 20.51 / 52.47	37.82 \pm 67.01	6.43	99.45	6.85 / 22.85 / 54.09	31.32 \pm 51.18	12.28
DINOV3 + XoFTR	91.66	1.66 / 7.11 / 21.36	172.17 \pm 291.38	1.20	96.77	2.04 / 8.21 / 23.32	128.96 \pm 233.40	1.41	99.53	2.17 / 9.36 / 25.57	95.59 \pm 177.26	2.19
DINOV3 + RoMa	91.66	3.87 / 14.38 / 38.85	57.81 \pm 82.84	4.20	96.77	5.02 / 16.68 / 42.77	47.77 \pm 71.82	6.52	99.53	5.02 / 18.72 / 44.64	40.09 \pm 57.15	12.11
DINOV3 + MINIMA _{RoMa}	91.66	5.49 / 18.68 / 49.15	50.82 \pm 91.57	4.34	96.77	4.89 / 20.21 / 53.06	37.66 \pm 67.04	7.41	99.53	6.64 / 20.81 / 53.45	29.19 \pm 43.97	12.53
SCC-Loc (Ours)	92.30	33.49 / 56.43 / 76.64	26.28 \pm 67.94	7.55	96.98	51.66 / 81.32 / 89.87	15.30 \pm 44.54	7.52	99.57	52.09 / 86.38 / 93.53	9.37 \pm 25.26	14.21

TABLE III

COMPARISON WITH DOMAIN-SPECIFIC BASELINES ACROSS VARYING SEARCH AREAS ON OUR THERMAL-UAV DATASET UNDER THE TOP-10 RETRIEVAL SETTING. BEST RESULTS ARE IN **BOLD**.

Method	Search Area: 600 \times 600			Search Area: 800 \times 800			Search Area: 1200 \times 1200			Memory
	Acc@5/10/20	ME \pm SD	Time	Acc@5/10/20	ME \pm SD	Time	Acc@5/10/20	ME \pm SD	Time	
NIVnet	0.10 / 0.80 / 2.60	91.64 \pm 35.06	0.02	0.10 / 0.60 / 2.10	92.37 \pm 35.63	0.03	0.20 / 0.70 / 1.90	99.21 \pm 47.49	0.04	15
STHN	0.50 / 3.10 / 11.50	40.70 \pm 15.49	0.03	0.70 / 3.10 / 12.10	38.76 \pm 16.57	0.03	1.00 / 3.40 / 12.00	49.60 \pm 44.40	0.04	5.5
DINOV2 + MINIMA _{RoMa}	6.85 / 22.85 / 54.09	31.32 \pm 51.18	12.28	6.26 / 20.89 / 52.51	36.92 \pm 73.59	12.50	5.11 / 19.06 / 48.13	69.05 \pm 148.08	13.62	2335.5
SCC-Loc (Ours)	52.09 / 86.38 / 93.53	9.37 \pm 25.26	14.21	51.40 / 81.70 / 89.87	16.84 \pm 55.63	14.30	46.30 / 76.00 / 83.45	46.62 \pm 127.04	16.12	1174.7

reveal several critical insights regarding the cross-modal geolocalization bottleneck.

1) The Modality Gap in Coarse Retrieval: Directly transferring visible-only models to thermal scenarios yields severe degradation. For instance, CAMP-based baselines achieve only 75.15% in Recall@3 due to the profound thermal-visible domain shift. Conversely, VFMs like DINOV2 and DINOV3 demonstrate robust zero-shot generalization, successfully bridging this semantic gap and boosting Recall@10 to > 99.45%.

2) The Fragility of Conventional Matchers: Precise geometric solving exposes the vulnerability of disjointed pipelines that rely solely on inlier counts. Confronted with repetitive topological visual decoys, incorrect candidates often yield deceptively high inliers, causing uniform matcher failure. Specifically, at Top-10, the intra-modal RoMa yields a mere 5.02% Acc@5 (with DINOV3), the cross-modal XoFTR suffers extreme geometric degradation (95.59 \pm 177.26 m mean error), and even the domain-adapted MINIMA_{RoMa} plateaus at 6.64%. This proves that implicitly trusting raw dense correspondences traps systems in a "low residual, high drift" state.

3) Effectiveness of the SCC-Loc Framework: SCC-Loc fundamentally resolves this bottleneck. By integrating semantic viewport alignment, cascaded filtering, and multi-dimensional reliability evaluation, we suppress the mean error to single digits (9.37 \pm 25.26 m at Top-10)—a 7.6 \times improvement at the strict 5-meter threshold over the strongest baseline (DINOV2 + MINIMA_{RoMa}). Furthermore, as the search pool expands from Top-3 to Top-10, baseline accuracy typically stagnates due to the influx of visual decoys. Conversely, our CD-RAPS strategy efficiently mines the true pose from these

noisier pools, surging SCC-Loc's Acc@5 from 33.49% to 52.09%.

4) Precision-Latency Trade-off: Regarding computational efficiency, rapid disjointed combinations like DINOV2 + XoFTR execute in merely 0.92 s/query but suffer catastrophic accuracy drops (1.66% Acc@5 at Top-3). While SCC-Loc requires marginally higher processing time than the strongest disjointed baseline (14.21 s compared to 12.28 s at Top-10), this latency is strictly allocated to our robust cascaded filtering and physically constrained optimization. By trading this marginal speed, SCC-Loc structurally eradicates geometric outliers, achieving an absolute localization accuracy fundamentally unattainable by conventional matchers.

C. Comparison against Domain-Specific Baselines

To further evaluate the effectiveness of the proposed SCC-Loc, we compare it with domain-specific networks STHN and NIVnet by expanding the search area from 600 \times 600 to 1200 \times 1200 m. The Top-10 retrieval results are summarized in Table III.

1) Brittleness of End-to-End Regression: Despite supervised training on Thermal-UAV, both STHN and NIVnet exhibit performance collapse in large-scale search spaces, with Acc@5 consistently \leq 1.00%. This failure stems from their reliance on direct parameter regression without hierarchical search, making them highly susceptible to initial viewpoint discrepancies and visual decoys in unconstrained global localization.

2) Robustness Against Scale Variations: As the search area quadruples (600 \times 600 to 1200 \times 1200 m), the strongest baseline (DINOV2 + MINIMA_{RoMa}) suffers severe degradation. In contrast, SCC-Loc demonstrates superior scalability.

TABLE IV

ABLATION STUDY OF THE PROPOSED FRAMEWORK UNDER THE TOP-5 RETRIEVAL SETTING. THE BEST RESULTS ARE HIGHLIGHTED IN **BOLD**.

Components			Performance Metrics			
SGVA	C-SATSF	CD-RAPS	Recall@5	Acc@5/10/20	ME \pm SD	Time
✓			96.98	5.91 / 23.49 / 56.38	33.74 \pm 61.53	6.81
	✓		96.72	7.15 / 21.87 / 53.40	37.40 \pm 68.48	6.82
		✓	96.72	17.40 / 46.47 / 74.72	26.08 \pm 55.59	8.60
✓	✓		96.98	8.00 / 24.47 / 57.70	32.73 \pm 60.38	7.00
✓		✓	96.98	20.89 / 51.91 / 78.00	21.71 \pm 46.61	8.58
	✓	✓	96.72	49.66 / 78.13 / 87.32	18.99 \pm 54.25	7.36
✓	✓	✓	96.98	51.66 / 81.32 / 89.87	15.30 \pm 44.54	7.52

Under the 1200×1200 m setting, it maintains a robust 46.30% Acc@5, alongside high Acc@10 (76.00%) and Acc@20 (83.45%). Although the mean error increases to 46.62 m due to positional drifts from a few unlocalized queries, the consistently high recall rates firmly validate that our proposed method remains highly effective and robust in large-scale search spaces.

3) Deployment Efficiency and Memory Advantage:

While end-to-end models offer rapid inference (≤ 0.04 s), their accuracy is insufficient for reliable deployment. Among viable two-stage paradigms, SCC-Loc presents a highly advantageous trade-off. Although our pipeline requires slightly higher latency (14.21 s compared to 12.28 s) for rigorous filtering and optimization, its unified architecture yields significant memory savings. By sharing a single-load DINOv2 backbone across both retrieval and matching stages, SCC-Loc restricts peak GPU memory to 1174.7 MB—effectively halving the 2335.5 MB overhead of disjointed baselines. This balance of geometric precision and resource efficiency is critical for deployment on constrained UAV platforms.

D. Ablation Study

To rigorously validate the individual and synergistic contributions of the proposed modules (SGVA, C-SATSF, and CD-RAPS) within the SCC-Loc framework, we conduct an ablation study under the Top-5 retrieval setting, with results detailed in Table IV.

1) Impact of Consensus-Driven Selection: CD-RAPS provides the most significant standalone improvement, achieving 17.40% Acc@5 and reducing ME to 26.08 m—outperforming standalone SGVA (5.91%) and C-SATSF (7.15%). This confirms that in selecting the optimal candidate location, replacing naive inlier counting with a geographic consensus voting mechanism—guided by multi-dimensional reliability evaluation and physical priors—is the most critical intervention for mitigating massive positional drift in cross-modal scenarios.

2) Synergy of Purification and Consensus: The coupling of C-SATSF and CD-RAPS yields a transformative performance leap, increasing Acc@5 from 17.40% to 49.66% and further compressing ME to 18.99 m. This synergy demonstrates that geographic consensus efficacy depends heavily

TABLE V

ROBUSTNESS EVALUATION OF THE PROPOSED FRAMEWORK UNDER VARYING PITCH AND YAW ANGLES IN THE TOP-5 RETRIEVAL SETTING.

Noise Config		Performance Metrics		
δ_{pitch}	δ_{yaw}	Recall@5	Acc@5/10/20	ME \pm SD
0	0	96.98	51.66 / 81.32 / 89.87	15.30 \pm 44.54
	10	97.36	51.02 / 82.00 / 89.70	15.42 \pm 44.24
	20	97.36	52.34 / 81.91 / 89.06	15.48 \pm 43.87
10	0	96.72	28.98 / 51.74 / 71.45	21.83 \pm 44.71
	10	97.19	28.17 / 51.66 / 70.51	22.31 \pm 44.87
	20	97.45	29.74 / 52.34 / 70.47	22.16 \pm 44.70
20	0	95.79	27.49 / 46.68 / 60.09	26.99 \pm 45.67
	10	96.55	26.55 / 46.26 / 58.81	28.61 \pm 48.92
	20	96.94	28.13 / 46.00 / 58.94	28.86 \pm 51.79

on correspondence quality and spatial distribution. By filtering low-texture ambiguities and topological distractors while ensuring a uniform distribution of the retained matches, C-SATSF provides a purified geometric foundation that prevents the CD-RAPS voting mechanism from being overwhelmed by structurally similar outliers or biased by locally clustered points.

3) Efficacy of Semantic Viewport Alignment: Building upon the synergistic foundation of C-SATSF and CD-RAPS, integrating SGVA completes the cohesive SCC-Loc architecture, achieving optimal overall performance. It not only minimizes the mean error to 15.30 m and yields a peak Acc@5 of 51.66%, but also maintains consistent improvements across all accuracy thresholds. Furthermore, it sustains the highest coarse retrieval recall (96.98%). SGVA effectively resolves spatial quantization bias inherent in grid-based database construction. By adaptively aligning the reference viewport with the UAV’s semantic field-of-view, it prevents target marginalization. This alignment ensures subsequent matching and optimization stages operate on optimally centered patches, establishing a robust, all-weather geo-localization paradigm.

4) Computational Efficiency: Standalone CD-RAPS incurs the highest latency (8.60 s) due to its iterative physics-constrained pose optimization. However, coupling it with C-SATSF reduces this time to 7.36 s. By filtering ambiguous outliers beforehand, C-SATSF provides a purified correspondence set that significantly accelerates the constrained solver’s convergence. Ultimately, the full SCC-Loc pipeline operates at 7.52 s, achieving an optimal trade-off between localization accuracy and computational efficiency.

E. Robustness Analysis

To evaluate SCC-Loc against telemetry deviations induced by sensor inaccuracies or wind disturbances, we inject uniformly distributed noise into the pitch (δ_{pitch}) and yaw (δ_{yaw}) priors. Table V details the Top-5 retrieval performance under varying noise configurations.

1) Resilience to Yaw Perturbations: Although SCC-Loc utilizes a yaw prior for initial North-alignment, it demonstrates exceptional robustness against inherent prior deviations. Evaluated with injected yaw noise (δ_{yaw}) up to 20° , performance variations remain marginal across all pitch configurations,

with Acc@R and mean errors maintaining high stability. This confirms that our DINOv2-based cascaded pipeline possesses sufficient rotational invariance to tolerate residual in-plane rotations caused by biased priors, ensuring accurate feature association and robust geometric solving.

2) Sensitivity to Pitch Distortions: Unlike yaw, pitch perturbations lead to a predictable performance decrease. As δ_{pitch} reaches 20° , Acc@5 drops to 28.13% and mean error rises to 28.86 m. This sensitivity stems from the dual role of the pitch prior in our framework. First, pitch is used to estimate the effective GSD for satellite patch cropping; biased priors cause cross-modal scale inconsistencies and viewport misalignments. Second, the CD-RAPS strategy employs the pitch prior as a physical penalty term in non-linear pose optimization. Severe noise misguides the objective function, forcing convergence toward geometrically biased configurations and amplifying position error.

Nevertheless, this represents a bounded degradation rather than systemic failure. Even under extreme dual-noise (20° pitch and 20° yaw), SCC-Loc bounds the mean error to under 30 m—still significantly outperforming conventional baselines operating under ideal, noise-free conditions.

VI. DISCUSSION

Our analysis indicates that the thermal-visible modality gap manifests as a **structural illusion**, where geographically distinct entities—such as repetitive rooftops or identical agricultural plots—exhibit near-identical thermal signatures. This inherent ambiguity frequently deceives local matchers into generating dense but spatially erroneous correspondences. Consequently, relying solely on correspondence cardinality for pose identification is inherently unreliable, as false candidates often accumulate deceptively high inlier counts. Our findings demonstrate that integrating explicit physical constraints, multi-dimensional reliability evaluation, and geographic consensus is indispensable for distinguishing the true global optimum from these pervasive visual decoys.

Despite these gains, SCC-Loc presents three primary limitations:

- **Hyperparameter Dependency:** The framework relies on a relatively large number of manually defined hyperparameters, making the initialization process complex.
- **Telemetry Sensitivity:** Satellite image partitioning during retrieval and pose optimization are coupled with initial pitch and yaw priors; telemetry inaccuracies (e.g., gimbal jitter) can distort alignment and degrade precision.
- **Inference Latency:** The sequential execution of matching, filtering, and optimization incurs computational overhead, challenging real-time edge deployment.

These bottlenecks suggest evolving SCC-Loc into a fully **end-to-end trainable architecture**. A unified framework could replace manual thresholds with learnable parameters and implicitly compensate for attitude variations through cross-modal feature correlations. Ultimately, distilling the multi-stage pipeline into a single-pass forward propagation will minimize latency, enabling efficient real-time deployment on resource-constrained UAVs.

VII. CONCLUSION

In this paper, we propose SCC-Loc, a unified Semantic-Cascade-Consensus framework for UAV cross-modal Thermal Geo-localization in GNSS-denied environments. By sharing a single-load foundation model across both retrieval and matching phases, SCC-Loc establishes a memory-efficient paradigm to elegantly bridge the profound modality gap. To systematically overcome spatial misalignments, massive structural outliers, and decoy-induced positional drift, we integrate the SGVA module, the C-SATSF mechanism, and the CD-RAPS strategy. Additionally, we construct the Thermal-UAV dataset, providing comprehensive multi-temporal and complex topological variations with aligned 3D priors to facilitate cross-modal benchmarking. Ultimately, this work advances automatic multimodal remote sensing image registration and cross-view image geolocation, validating thermal imagery as a robust, complementary source for Earth observation and all-weather autonomous UAV navigation.

REFERENCES

- [1] I. Martinez-Alpiste, G. Golcarenenji, Q. Wang, and J. M. Alcaraz-Calero, "Search and rescue operation using uavs: A case study," *Expert Syst. Appl.*, vol. 178, p. 114937, 2021.
- [2] R. Koslowski, "Drones and border control: An examination of state and non-state actor use of uavs along borders," in *Research Handbook on International Migration and Digital Technology*. Edward Elgar Publishing, 2021, pp. 152–165.
- [3] Z. Zheng, Y. Wei, and Y. Yang, "University-1652: A multi-view multi-source benchmark for drone-based geo-localization," in *Proc. ACM Int. Conf. Multimedia*, 2020, pp. 1395–1403.
- [4] A. Couturier and M. A. Akhloufi, "A review on deep learning for uav absolute visual localization," *Drones*, vol. 8, no. 11, p. 622, 2024.
- [5] J. Xiao, D. Tortei, E. Roura, and G. Loianno, "Long-range uav thermal geo-localization with satellite imagery," in *Proc. IEEE/RSJ Int. Conf. Intell. Robots Syst. (IROS)*. IEEE, 2023, pp. 5820–5827.
- [6] J. Xiao, N. Zhang, D. Tortei, and G. Loianno, "Sthn: Deep homography estimation for uav thermal geo-localization with satellite imagery," *IEEE Robot. Autom. Lett.*, 2024.
- [7] J. Xiao and G. Loianno, "Uasthn: Uncertainty-aware deep homography estimation for uav satellite-thermal geo-localization," in *Proc. IEEE Int. Conf. Robot. Autom. (ICRA)*. IEEE, 2025, pp. 14 066–14 072.
- [8] M. He, J. Liu, P. Gu, and Z. Meng, "Leveraging map retrieval and alignment for robust uav visual geo-localization," *IEEE Trans. Instrum. Meas.*, vol. 73, pp. 1–13, 2024.
- [9] Y. Ye, X. Teng, S. Chen, Z. Li, L. Liu, Q. Yu, and T. Tan, "Exploring the best way for uav visual localization under low-altitude multi-view observation condition: a benchmark," *arXiv:2503.10692*, 2025.
- [10] X. Meng, W. Guo, K. Zhou, T. Sun, L. Deng, S. Yu, and Y. Feng, "Airgeonet: A map-guided visual geo-localization approach for aerial vehicles," *IEEE Trans. Geosci. Remote Sens.*, 2024.
- [11] Ö. Tuzcuoğlu, A. Köksal, B. Sofu, S. Kalkan, and A. A. Alatan, "Xoftr: Cross-modal feature matching transformer," in *Proc. IEEE/CVF Conf. Comput. Vis. Pattern Recognit. (CVPR)*, 2024, pp. 4275–4286.
- [12] R. Wu, J. Deng, M. Mou, X. He, M. Zhang, Y. Liu, and S. Yan, "Uav-geoloc: A large-vocabulary dataset and geometry-transformed method for uav geo-localization," *IEEE Robot. Autom. Lett.*, 2025.
- [13] Y. Ji, B. He, Z. Tan, and L. Wu, "Game4loc: A uav geo-localization benchmark from game data," in *Proc. AAAI Conf. Artif. Intell.*, vol. 39, no. 4, 2025, pp. 3913–3921.
- [14] W. Xu, Y. Yao, J. Cao, Z. Wei, C. Liu, J. Wang, and M. Peng, "Uav-visloc: A large-scale dataset for uav visual localization," *arXiv:2405.11936*, 2024.
- [15] R. Zhu, L. Yin, M. Yang, F. Wu, Y. Yang, and W. Hu, "Sues-200: A multi-height multi-scene cross-view image benchmark across drone and satellite," *IEEE Trans. Circuits Syst. Video Technol.*, vol. 33, no. 9, pp. 4825–4839, 2023.
- [16] M. Dai, E. Zheng, Z. Feng, L. Qi, J. Zhuang, and W. Yang, "Vision-based uav self-positioning in low-altitude urban environments," *IEEE Trans. Image Process.*, vol. 33, pp. 493–508, 2023.

- [17] D. Avola, L. Cinque, E. Emam, F. Fontana, G. L. Foresti, M. R. Marini, A. Mecca, and D. Pannone, "Uav geo-localization for navigation: A survey," *IEEE Access*, 2024.
- [18] Y. Ji, B. He, Z. Tan, and L. Wu, "Mmgeo: Multimodal compositional geo-localization for uavs," in *Proc. IEEE/CVF Int. Conf. Comput. Vis. (ICCV)*, 2025, pp. 25 165–25 175.
- [19] R. Arandjelovic, P. Gronat, A. Torii, T. Pajdla, and J. Sivic, "Netvlad: Cnn architecture for weakly supervised place recognition," in *Proc. IEEE Conf. Comput. Vis. Pattern Recognit. (CVPR)*, 2016, pp. 5297–5307.
- [20] M. Dai, J. Hu, J. Zhuang, and E. Zheng, "A transformer-based feature segmentation and region alignment method for uav-view geo-localization," *IEEE Trans. Circuits Syst. Video Technol.*, vol. 32, no. 7, pp. 4376–4389, 2021.
- [21] Q. Wu, Y. Wan, Z. Zheng, Y. Zhang, G. Wang, and Z. Zhao, "Camp: A cross-view geo-localization method using contrastive attributes mining and position-aware partitioning," *IEEE Trans. Geosci. Remote Sens.*, 2024.
- [22] X. Liu, Z. Wang, Y. Wu, and Q. Miao, "Segcn: A semantic-aware graph convolutional network for uav geo-localization," *IEEE J. Sel. Top. Appl. Earth Observ. Remote Sens.*, vol. 17, pp. 6055–6066, 2024.
- [23] N. Keetha, A. Mishra, J. Karhade, K. M. Jatavallabhula, S. Scherer, M. Krishna, and S. Garg, "Anyloc: Towards universal visual place recognition," *IEEE Robot. Autom. Lett.*, vol. 9, no. 2, pp. 1286–1293, 2023.
- [24] O. Siméoni, H. V. Vo, M. Seitzer, F. Baldassarre, M. Oquab, C. Jose, V. Khalidov, M. Szafraniec, S. Yi, M. Ramamonjisoa *et al.*, "Dinov3," *arXiv:2508.10104*, 2025.
- [25] J.-C. Yoo and T. H. Han, "Fast normalized cross-correlation," *Circuits, Syst. Signal Process.*, vol. 28, no. 6, pp. 819–843, 2009.
- [26] D. DeTone, T. Malisiewicz, and A. Rabinovich, "Superpoint: Self-supervised interest point detection and description," in *Proc. IEEE Conf. Comput. Vis. Pattern Recognit. Workshops*, 2018, pp. 224–236.
- [27] J. Sun, Z. Shen, Y. Wang, H. Bao, and X. Zhou, "Loftr: Detector-free local feature matching with transformers," in *Proc. IEEE/CVF Conf. Comput. Vis. Pattern Recognit. (CVPR)*, 2021, pp. 8922–8931.
- [28] J. Edstedt, Q. Sun, G. Bökman, M. Wadenbäck, and M. Felsberg, "Roma: Robust dense feature matching," in *Proc. IEEE/CVF Conf. Comput. Vis. Pattern Recognit. (CVPR)*, 2024, pp. 19 790–19 800.
- [29] J. Ren, X. Jiang, Z. Li, D. Liang, X. Zhou, and X. Bai, "Minima: Modality invariant image matching," in *Proc. Comput. Vis. Pattern Recognit. Conf. (CVPR)*, 2025, pp. 23 059–23 068.
- [30] J. Chen, E. Zheng, M. Dai, Y. Chen, and Y. Lu, "Os-fpi: A coarse-to-fine one-stream network for uav geolocalization," *IEEE J. Sel. Top. Appl. Earth Observ. Remote Sens.*, vol. 17, pp. 7852–7866, 2024.
- [31] W. Xu, N. Chen, J. Yuan, J. Fan, W. Chen, and E. Zheng, "Enhancing uav geo-location with multi-modal transformer networks: The mmgl approach," *IEEE J. Sel. Top. Appl. Earth Observ. Remote Sens.*, 2026.
- [32] C.-E. Vasile, C. Bîră, and R. Hobincu, "Uav-tirvis: A benchmark dataset for thermal-visible image registration from aerial platforms," *J. Imag.*, vol. 11, no. 12, p. 432, 2025.
- [33] J. Liu, C. Zhao, C. Zhao, N. Su, W. Lu, Y. Yan, S. Feng, and Y. Qu, "Mcgs-reid: A visible-infrared vehicle reidentification method using modal-cross graph sampler," *IEEE J. Sel. Top. Appl. Earth Observ. Remote Sens.*, vol. 18, pp. 18 806–18 818, 2024.
- [34] Z. Liu, H. Li, Z. Zhang, Y. Lyu, and J. Xiong, "Multimodal absolute visual localization for unmanned aerial vehicles," *IEEE Trans. Veh. Technol.*, vol. 73, no. 11, pp. 16 402–16 415, 2024.
- [35] M. Oquab, T. Darcet, T. Moutakanni, H. Vo, M. Szafraniec, V. Khalidov, P. Fernandez, D. Haziza, F. Massa, A. El-Nouby *et al.*, "Dinov2: Learning robust visual features without supervision," *arXiv:2304.07193*, 2023.
- [36] F. Radenović, G. Toliás, and O. Chum, "Fine-tuning cnn image retrieval with no human annotation," *IEEE Trans. Pattern Anal. Mach. Intell.*, vol. 41, no. 7, pp. 1655–1668, 2018.
- [37] A. Dosovitskiy, "An image is worth 16x16 words: Transformers for image recognition at scale," *arXiv:2010.11929*, 2020.
- [38] Y. Wu and Z. Hu, "Pnp problem revisited," *J. Math. Imag. Vis.*, vol. 24, no. 1, pp. 131–141, 2006.
- [39] J. Ma, J. Zhao, J. Jiang, H. Zhou, and X. Guo, "Locality preserving matching," *Int. J. Comput. Vis.*, vol. 127, no. 5, pp. 512–531, 2019.
- [40] S. Jiang and W. Jiang, "Reliable image matching via photometric and geometric constraints structured by delaunay triangulation," *ISPRS J. Photogrammetry Remote Sens.*, vol. 153, pp. 1–20, 2019.
- [41] S. Lowry, N. Sünderhauf, P. Newman, J. J. Leonard, D. Cox, P. Corke, and M. J. Milford, "Visual place recognition: A survey," *IEEE Trans. Robot.*, vol. 32, no. 1, pp. 1–19, 2015.
- [42] T. Qin, P. Li, and S. Shen, "Vins-mono: A robust and versatile monocular visual-inertial state estimator," *IEEE Trans. Robot.*, vol. 34, no. 4, pp. 1004–1020, 2018.
- [43] J. Sola, J. Deray, and D. Atchuthan, "A micro lie theory for state estimation in robotics," *arXiv:1812.01537*, 2018.
- [44] S. K. Sengijpta, "Fundamentals of statistical signal processing: Estimation theory," 1995.
- [45] J. Zhang, M. Kaess, and S. Singh, "On degeneracy of optimization-based state estimation problems," in *Proc. IEEE Int. Conf. Robot. Autom. (ICRA)*. IEEE, 2016, pp. 809–816.
- [46] O. Dhaouadi, R. Marin, J. Meier, J. Kaiser, and D. Cremers, "Ortholoc: Uav 6-dof localization and calibration using orthographic geodata," *arXiv:2509.18350*, 2025.
- [47] C. Li, M. He, C. Chen, J. Liu, X. Lyu, G. Huang, and Z. Meng, "Geoivins: Geographic-visual-inertial navigation system for large-scale drift-free aerial state estimation," *IEEE Trans. Robot.*, 2025.



Xiaoran Zhang received the B.E. degree in simulation engineering from the National University of Defense Technology, Changsha, China, in 2024, where he is currently pursuing the M.S. degree in control science and engineering.

His research interests include unmanned systems, visual geo-localization and computer vision.



Yu Liu received the B.E. degree in management science and engineering from the National University of Defense Technology, Changsha, China, in 2024, where he is currently pursuing the M.S. degree in control science and engineering.

His research interests include visual geo-localization and computer vision.



Jinyu Liang received the B.E. degree in automation from the Central South University of Forestry and Technology, Changsha, China, in 2024, where he is currently pursuing the M.S. degree in control science and engineering.

His research interests include image recognition and 3D reconstruction.



Kangqiushi Li received the B.E. degree in simulation engineering from the National University of Defense Technology, Changsha, China, in 2024, where he is currently pursuing the M.S. degree in electronic information.

His research interests include target detection and computer vision.



Zhiwei Huang received the B.E. degree in management science and engineering from the National University of Defense Technology, Changsha, China, in 2025, where he is currently pursuing the M.S. degree in control science and engineering.

His research interests include fast 3D reconstruction and computer vision.



Huaxin Xiao received the Ph.D. degree from the National University of Defense Technology, Changsha, China, in 2018. He is currently an Associate Professor with the College of System Engineering, National University of Defense Technology.

His current research interests include saliency detection and image/video object segmentation.